



Article

Preparation of Fe@Fe₃O₄/ZnFe₂O₄ Powders and Their Consolidation via Hybrid Cold-Sintering/Spark Plasma-Sintering

Amalia Mesaros ^{1,*}, Bogdan Viorel Neamtu ², Traian Florin Marinca ², Florin Popa ², Gabriela Cupa ², Otilia Ruxandra Vasile ³ and Ionel Chicinas ^{2,*}

¹ Physics and Chemistry Department, Technical University of Cluj-Napoca, 103-105 Muncii Avenue, 400641 Cluj-Napoca, Romania

² Materials Science and Engineering Department, Technical University of Cluj-Napoca, 103-105 Muncii Avenue, 400641 Cluj-Napoca, Romania; bogdan.neamtu@stm.utcluj.ro (B.V.N.); traian.marinca@stm.utcluj.ro (T.F.M.); florin.popa@stm.utcluj.ro (F.P.)

³ Department of Science and Engineering of Oxide Materials and Nanomaterials, Faculty of Chemical Engineering and Biotechnologies, National University of Science and Technology Politehnica Bucharest, No 1-7 Polizu Street, S1, 060042 Bucharest, Romania; otilia.vasile@upb.ro

* Correspondence: amalia.mesaros@chem.utcluj.ro (A.M.); ionel.chicinas@stm.utcluj.ro (I.C.)

Abstract: Our study is focused on optimizing the synthesis conditions for the in situ oxidation of Fe particles to produce Fe@Fe₃O₄ core-shell powder and preparation via co-precipitation of ZnFe₂O₄ nanoparticles to produce Fe@Fe₃O₄/ZnFe₂O₄ soft magnetic composites (SMC) through a hybrid cold-sintering/spark plasma-sintering technique. XRD and FTIR measurements confirmed the formation of a nanocrystalline oxide layer on the surface of Fe powder and the nanosized nature of ZnFe₂O₄ nanoparticles. SEM-EDX investigations revealed that the oxidic phase of our composite was distributed on the surface of the Fe particles, forming a quasi-continuous matrix. The DC magnetic characteristics of the composite compact revealed a saturation induction of 0.8 T, coercivity of 590 A/m, and maximum relative permeability of 156. AC magnetic characterization indicated that for frequencies higher than 1 kHz and induction of 0.1 T, interparticle eddy current losses dominated due to ineffective electrical insulation between neighboring particles in the composite compact. Nevertheless, the magnetic characteristics obtained in both DC and AC magnetization regimes were comparable to those reported for cold-sintered Fe-based SMCs.

Keywords: in situ oxidation; Fe@Fe₃O₄ core-shell powder; ZnFe₂O₄ nanoparticles; soft magnetic composite; cold-sintering/spark plasma-sintering



Citation: Mesaros, A.; Neamtu, B.V.; Marinca, T.F.; Popa, F.; Cupa, G.; Vasile, O.R.; Chicinas, I. Preparation of Fe@Fe₃O₄/ZnFe₂O₄ Powders and Their Consolidation via Hybrid Cold-Sintering/Spark Plasma-Sintering. *Nanomaterials* **2024**, *14*, 149. <https://doi.org/10.3390/nano14020149>

Academic Editors: Qifeng Ruan and Hao Wang

Received: 18 November 2023

Revised: 28 December 2023

Accepted: 30 December 2023

Published: 10 January 2024



Copyright: © 2024 by the authors. Licensee MDPI, Basel, Switzerland. This article is an open access article distributed under the terms and conditions of the Creative Commons Attribution (CC BY) license (<https://creativecommons.org/licenses/by/4.0/>).

1. Introduction

Soft magnetic composites (SMCs) constitute a significant subclass of the soft magnetic materials field due to their specific capability to produce innovative three-dimensional cores with high magnetic flux density and also due to their potential utilization in various electrical machinery fields [1–4]. In recent decades, researchers have focused on the enhancement of the magnetic properties of SMCs by studying the effects induced by the thin insulating layer on the surface and by optimizing their elaboration technology [4–8]. An organic insulating layer limits the thermal treatment temperature of SMCs, while an inorganic coating such as Al₂O₃, SiO₂, or ZrO₂ degrades the saturation magnetization due to the magnetic dilution effect induced by the non-magnetic insulating layer [9–15]. To overcome these deficiencies, ferromagnetic materials such as ferrite-type systems, Mn-Zn ferrites, Ni-Zn ferrites, and Fe_xO_y (especially Fe₃O₄) have been considered as the suitable insulating layer [8,16–23]. Additionally, several studies present the elaboration of SMCs with an inorganic double-insulating layer that enhances heat resistance and enables enhanced magnetic and mechanical performance by high-temperature annealing [4,24,25].

To date, different wet chemical methods such as sol-gel, co-precipitation, hydrothermal or dry strategies, mechanical alloying, and atmosphere oxidation have been developed for the synthesis of composite particles. Even if the dry methods are more facile, their efficiency is lower than the wet chemical approach because it is difficult to form a uniform coating layer on the surface of soft magnetic particles. Additionally, many efforts have been made to control layer thickness and reduce the defects or holes from the interface between the ferrite or oxide layer and metal, drastically diminishing the composite properties [1–6]. The melting point, resistivity, and bandgap energy are important characteristics of the coating layer. A high-quality and uniform insulating layer effectively reduces eddy current losses by providing the material with remarkable insulation properties of resistivity and bandgap energy [4]. Recently, Zhang et al. reported that the in situ oxidation method assures the formation of a uniform Fe_3O_4 surface coating layer and, moreover, this method facilitates good control over the layer thickness [3]. The co-precipitation method was used by Yi et al. to grow a uniform $(\text{NiZn})\text{Fe}_2\text{O}_4$ layer on the surface of Fe particles, and the correlation between the structures and magnetic properties was deeply studied [26]. In addition to conventional strategies, the addition of inorganic particles, such as ZrO_2 , Al_2O_3 , MgO , Fe_3O_4 , and ZnSO_4 , has been considered to increase the electric resistance and lower the eddy current loss of SMCs [1,15,27–30]. As chemical methods for the elaboration of inorganic particles, it must be mentioned that sol-gel, precipitation/co-precipitation, or hydrothermal methods are often utilized. Between these chemical strategies, chemical precipitation is simple, less expensive, eco-friendly, allows an easy scale-up method, and assures the formation of homogeneous particles [31,32].

In this study, a step-by-step hybrid strategy was used to fabricate $\text{Fe@Fe}_3\text{O}_4/\text{ZnFe}_2\text{O}_4$ SMCs. In the first stage, $\text{Fe@Fe}_3\text{O}_4$ core-shell composites were obtained using an in situ surface oxidation method based on the reaction between Fe powder and O_2 in a weak acidic media. Additionally, ZnFe_2O_4 nanoparticles (ZFnps) were synthesized using a co-precipitation method at room temperature, under pH control, without any thermal treatment. The coating process that we used ensures the complete coating of the Fe particles with a layer of Fe_3O_4 . However, the thickness of the Fe_3O_4 layer is low, leading to the risk of electrical contact between Fe cores. To minimize this risk, a second insulating phase was added. It is worth mentioning that the electrical resistivity of Zn ferrite is approximately $1 \Omega \cdot \text{m}$ and the electrical resistivity of iron ferrite is only $4 \times 10^{-5} \Omega \cdot \text{m}$. In the second stage, the $\text{Fe@Fe}_3\text{O}_4$ composites and ZFnps were mixed and pressed to obtain a green compact. This compact was subjected to a hybrid cold-sintering/spark plasma-sintering process. No binder was added during the cold-sintering process in order to prevent the negative effects of the organic decomposition. FTIR and XRD investigation techniques have been used to evidence the formation of an oxide layer at the surface of Fe powder and to determine the optimum synthesis parameters for the ZFnps. $\text{Fe@Fe}_3\text{O}_4/\text{ZnFe}_2\text{O}_4$ soft magnetic composite was prepared via a hybrid cold-sintering/spark plasma-sintering process. The AC and DC magnetic characteristics of the composite are presented and discussed in light of the parameters of the preparation technique.

2. Experimental

2.1. Materials

Commercial iron powder (NC 100.24 type produced by Höganäs), Zinc acetate dihydrate, $\text{Zn}(\text{CH}_3\text{COO})_2 \cdot 2\text{H}_2\text{O}$ (99.9%, Merck, Darmstadt, Germany), iron (III) nanohydrate, $\text{Fe}(\text{NO}_3)_3 \cdot 9\text{H}_2\text{O}$ (99.9% Merck), sodium hydroxide and NaOH (pellets, Merck), hydrochloric acid, HCl (fuming 37%, Merck), and ethyl alcohol, $\text{C}_2\text{H}_5\text{OH}$ (pure, Merck), were used without any further purification.

2.1.1. Synthesis of the $\text{Fe@Fe}_3\text{O}_4$ Core-Shell Particles

The surface oxidation of Fe particles was achieved by an in situ oxidation method using an oxygen flow. A total of 10 g of iron powder were added under mechanical agitation to a mixture of 0.1 M HCl and 0.1 M KCl solutions heated to 60 °C. An oxygen gaseous

phase was introduced into the solution with a flow rate of 20 sccm for 20 min. The obtained particles were separated in a magnetic field, washed several times with distilled water until Cl^- ion-free, and dried at 50 °C for 3 h.

2.1.2. Synthesis of ZnFe_2O_4 Nanoparticles

The ZnFe_2O_4 spinel material was synthesized via the co-precipitation method using the simultaneous addition of reagent techniques (SimAdd) [33]: zinc acetate and iron (III) nitrate as the corresponding starting metal salts and sodium hydroxide as a precipitating reagent. The stoichiometric ratio of Zn^{2+} to Fe^{3+} ions was 1:2 in the initial 0.1 M aqueous solutions. Precipitation was carried out under continuous magnetic stirring, and the mixture of the metal–salt solutions and 1M NaOH aqueous solution were simultaneously added into 1:10 diluted metal precursor solution using a peristaltic pump. Precipitation was carried out under continuous stirring and pH control between 6–10 at room temperature. Each pH value was maintained during the precipitation reaction. The post-precipitation stage consisted of 24 h aging, separation by filtering, washing three times with distilled water, and drying at 80 °C for 8 h.

2.1.3. Elaboration of $\text{Fe@Fe}_3\text{O}_4/\text{ZnFe}_2\text{O}_4$ Toroidal-Shaped Magnetic Core

First, a mixture of $\text{Fe@Fe}_3\text{O}_4$ core–shell particles with 5 wt.% ZnFe_2O_4 nanoparticles (pH = 7) were prepared using a mortar and pestle. To facilitate the mixing and cold-sintering processes, several milliliters of ethyl alcohol were added to the powder prior to mixing. After 5 min of mixing, the wet powder was placed in a toroidal mold and punched and compacted at a compaction pressure of 500 MPa. The obtained compact (green compact) was subjected to a spark plasma sintering (SPS) process. The sintering experiments were conducted using homemade spark plasma sintering equipment. The process involved maintaining a temperature of 250 °C for 10 min, with a heating rate of 100 °C per minute. A pressure of 25 MPa was applied during sintering, and an argon gas atmosphere was employed for protection. A distinctive feature of our SPS technique was the use of a graphite die partially filled with fine graphite powder, with the sample immersed within it. This graphite powder effectively acted as a pseudo-liquid, ensuring an even distribution of the compaction pressure across the entire surface of the sample, similar to the principles of hot isostatic pressing. The choice of graphite powder was based on its electrical conductivity and anti-friction properties. To apply the compaction pressure of 25 MPa, a set of graphite punches was utilized, maintaining a constant pressure throughout the sintering process. After sintering was complete, the sample was removed from the graphite die and carefully cleaned to eliminate any adhering graphite particles.

2.2. Characterization Techniques

The chemical nature of the $\text{Fe@Fe}_3\text{O}_4$ core–shell system and ZnFe_2O_4 particles was analyzed by Fourier transform infrared spectroscopy (FTIR) using a Tensor 27 Bruker FTIR spectrophotometer (Markham, ON, Canada). The morphology of the cold-sintered compact was investigated via scanning electron microscopy (SEM) and energy dispersive X-ray spectroscopy (EDX). The equipment that was used was a JEOL microscope, type JSM 5600LV, equipped with Ultim Max65 X-ray energy dispersive detectors from Oxford Instruments (Aztech software). Additionally, for the TEM investigation, a Tecnai G2 F30 S-TWIN transmission electron microscope at an accelerating voltage of 300 kV was used. The structural characterization of the core–shell particles ($\text{Fe}/\text{Fe}_3\text{O}_4$) and ZnFe_2O_4 nanoparticles were made by X-ray diffraction (XRD). The equipment used was an INEL Equinox 3000 diffractometer. The wavelength used was the one characteristic of Co , $\text{K}\alpha$ radiation ($\lambda = 1.7903 \text{ \AA}$). The mean crystallite size was calculated by the Scherrer method.

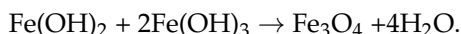
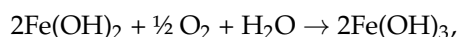
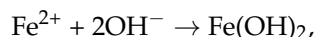
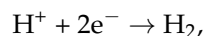
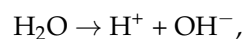
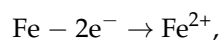
The magnetic characteristics of the toroidal-shaped magnetic core were assessed using a computer-controlled Remagraph–Remacomp C-705 hysteresisgraph manufactured by Magnet-Physik Dr. Steingroever GmbH (Hannover, Germany), Hannover, Germany. The magnetic characteristics were measured in both static (DC) and dynamic (AC) mag-

netization regimes. For DC measurements, the maximum field applied was 8.5 kA/m. AC magnetic measurements were carried out under a constant induction value (B_{\max}) of 0.1 T, covering a frequency range from 50 Hz to 10 kHz. The electrical resistivity of the toroidal-shaped magnetic core was measured using a four-point probe measurement setup.

3. Results and Discussion

3.1. Fe@Fe₃O₄ Core-Shell Powders

The chemical processes behind the formation of the oxidized layer at the surface of iron particles were studied and explained based on the iron corrosion theory [3]. Oxidation of the iron surface at high temperatures and under acidic media is favored by the presence of oxygen. The first process involved the transfer of electrons due to the oxidation of the Fe atom with the formation of Fe²⁺, followed by a reduction in H⁺ with the formation of H₂. Concurrently, the water ionization process took place with the formation of OH⁻ and H⁺ ions. Additionally, the oxidation of Fe²⁺ to Fe³⁺ was possible due to the presence of water and oxygen and all ionic entities chemically reacted with the formation of Fe₃O₄. The oxidation of Fe particle surface can be explained based on the following chemical reactions [3]:



In our work, the formation of the oxide layer on the surface of the Fe particles was investigated by FTIR and XRD measurements, as shown in Figure 1. The XRD pattern of the Fe@Fe₃O₄ system is presented in Figure 1a. There are three main diffraction lines at 52.5°, 77.4°, and 99.8°, corresponding to the (110), (200), and (211) planes of the α -Fe powder (JCPDS file no. 06-0696). Low-intensity additional lines (*) can be noticed, corresponding to the (220), (311), (400), (422), (511), (440), and (533) planes of the Fe₃O₄ cubic spinel structure (JCPDS file no. 19-0629). Additional peaks representing supplementary phases were not observed. Additionally, our oxidized powder presented a significant color change from silver to black, indicating the emergence of the Fe₃O₄ coating on the surface. The mean crystallite size of the Fe₃O₄ layer, calculated using the (311), (440), and (533) reflections, was 20 ± 2 nm.

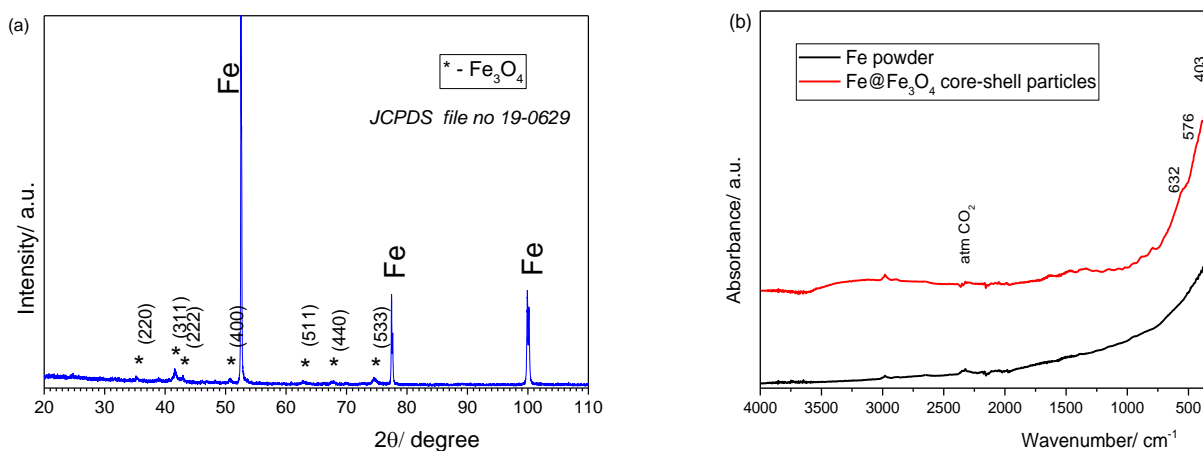


Figure 1. XRD pattern (a) and FTIR spectra (b) of Fe powder and the Fe@Fe₃O₄ system after 20 min in situ oxidation of iron powder.

The FTIR spectra of the iron powder before and after in situ oxidation are shown in Figure 1b. The three intense peaks observed at 403 cm^{-1} , 576 cm^{-1} , and 632 cm^{-1} are attributed to the vibration modes associated with the Fe-O bonds in the crystalline lattice of Fe_3O_4 . Low-intensity bands can be observed at approximately 1630 cm^{-1} and 340 cm^{-1} related to OH-bending and OH-stretching in the hydroxyl group [34]. From the above-discussed results, it can be concluded that a $\text{Fe}@\text{Fe}_3\text{O}_4$ composite system was formed.

SEM-EDX investigations were performed in order to present the morphology of the coated and uncoated Fe particles, as shown in Figure 2. It can be noticed that a uniform layer of oxide was formed by the chemical coating of Fe particles. As revealed by the XRD investigation, the oxide layer consists of a Fe_3O_4 phase.

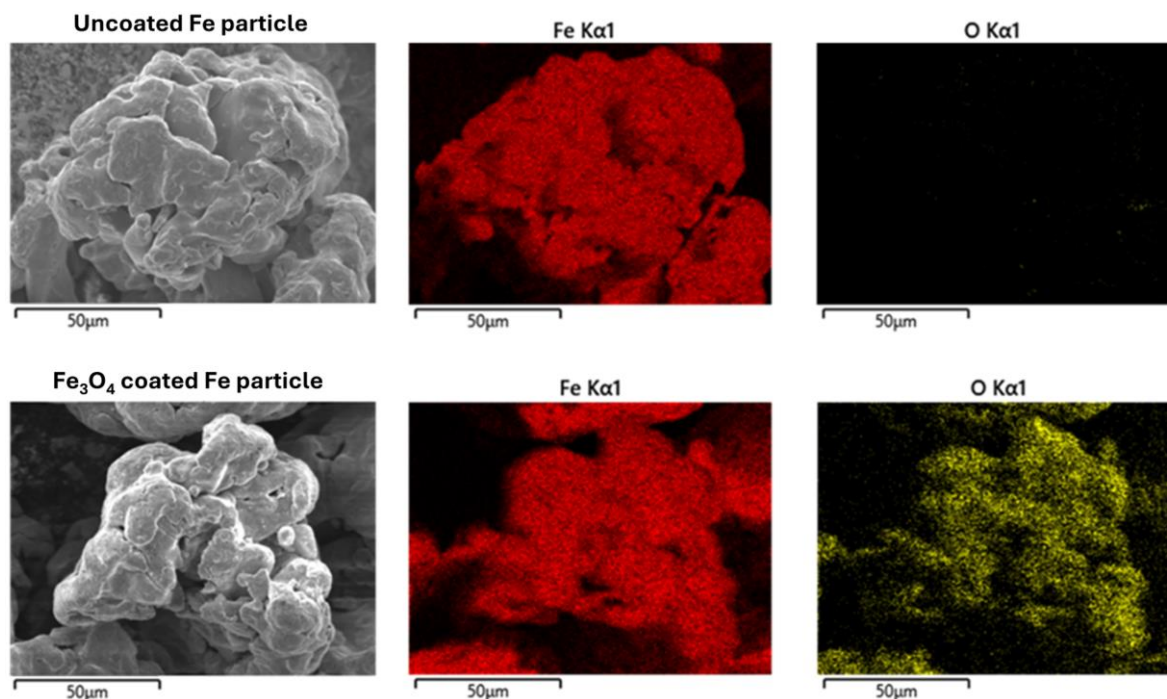
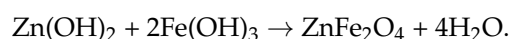
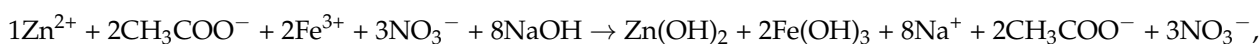


Figure 2. SEM-EDX analysis of the uncoated and Fe_3O_4 -coated particles.

3.2. ZnFe_2O_4 Nanoparticles

It is generally accepted that the chemical mechanism is crucial in studying and controlling the precipitation/co-precipitation process by SimAdd techniques [34,35]. The formation of ZnFe_2O_4 product during the co-precipitation processes of Zn^{2+} and Fe^{3+} ions with NaOH is governed by the following chemical reaction:



The structural characteristics of ZnFe_2O_4 samples obtained at different pH values of the precipitation media were determined by XRD measurements, as shown in Figure 3a. The diffraction patterns reveal the presence of the reflection lines corresponding to the spinel cubic structure of ZnFe_2O_4 for the four samples (JCPDS card no 22-1012). A supplementary phase attributed to the NaNO_3 crystalline structure (JCPDS card no. 36-1474) can be noticed for the samples obtained when the precipitation media are under basic pH conditions. This can be explained by the addition of a large amount of the precipitating agent, which leads to the formation of sodium salts, e.g., acetates and nitrates, as the secondary products, as reaction (2) suggests. The washing procedure assumes the removal of these supplementary products from the solution that contains a large amount of sodium salts. Since sodium

acetate presents higher solubility in water, it is removed first, and then sodium nitrate can partially remain crystallized on the ZnFe_2O_4 surface. The presence of nitrate ions in the samples obtained in basic media was confirmed by FTIR spectra, Figure 3b, through the presence of a low-intensity peak from 835 cm^{-1} , characteristic for the symmetric stretching vibration of the N-O bond in NO_3^- [36].

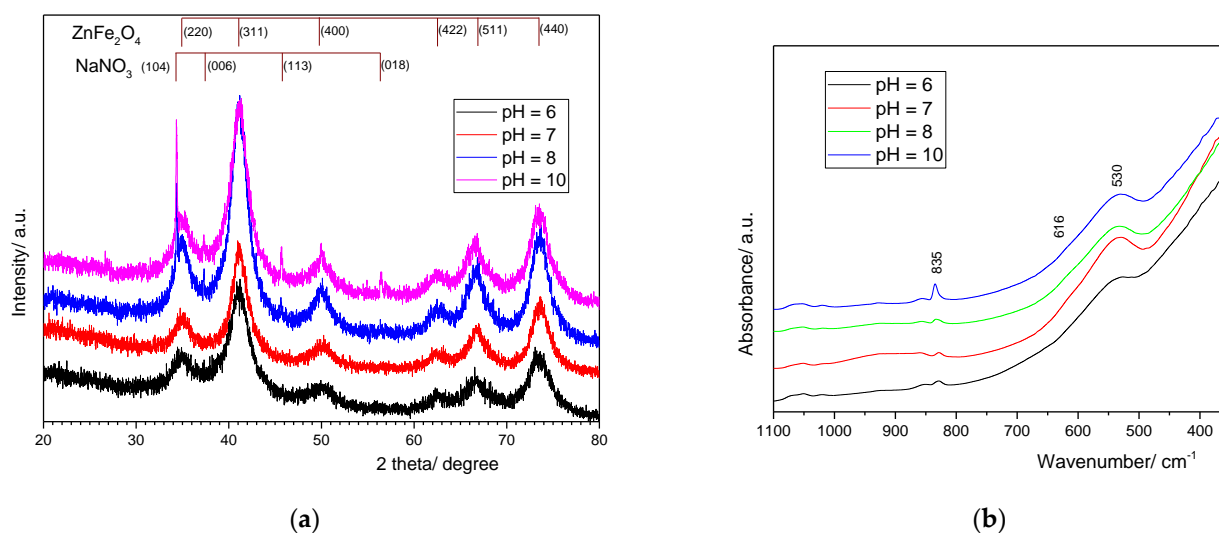


Figure 3. XRD patterns (a) and FTIR spectra (b) of the ZnFe_2O_4 samples synthesized at different pH values of precipitation media.

Additionally, the XRD measurements are indicative of the distribution of the Zn^{2+} to Fe^{3+} ions in the cubic spinel structure between tetrahedral and octahedral positions. It is well known that a normal cubic spinel structure is obtained when Zn^{2+} cations occupy tetrahedral positions. On the contrary, an inversed spinel structure is formed when Zn^{2+} cations prefer octahedral sites, and in terms of the lattice parameter, a value lower than 8.44 \AA , characteristic for Fe_3O_4 , is obtained [37]. The calculated lattice parameters for the four samples (Table 1) suggest that an inversed spinel structure is formed when the precipitation takes place at neutral pH. A weak acidic media (pH = 6) or a basic pH domain (pH = 12) leads to an increase in lattice parameters, suggesting that a normal spinel structure is formed. Additionally, broad XRD patterns reveal that the obtained ferrite particles are nanosized. The mean crystallite size, calculated through the Scherrer method applied to the (311), (511), and (440) reflections (Table 1), suggests that a neutral pH promotes the acceleration of the growth phase.

Table 1. Lattice parameter (a) and crystallite mean size (D) calculated from the XRD patterns for the samples synthesized at different pH values for the precipitation process.

ZnFe_2O_4 Sample	a (nm)	D (nm)
pH6	8.4522	3.8
pH7	8.4389	5.2
pH8	8.4498	5.1
pH10	8.4636	4.7

The morphological characteristics for ZnFe_2O_4 particles obtained at neutral pH (pH = 7) were investigated by TEM and are presented in Figure 4. The TEM image illustrates the formation of spherical-shaped, small, and agglomerated zinc ferrite nanoparticles. The ZnFe_2O_4 particle size, as revealed by TEM, is approximately 5–6 nm. This indicates that the ZnFe_2O_4 nanoparticles consist of one crystallite if the TEM data are correlated with the XRD data.

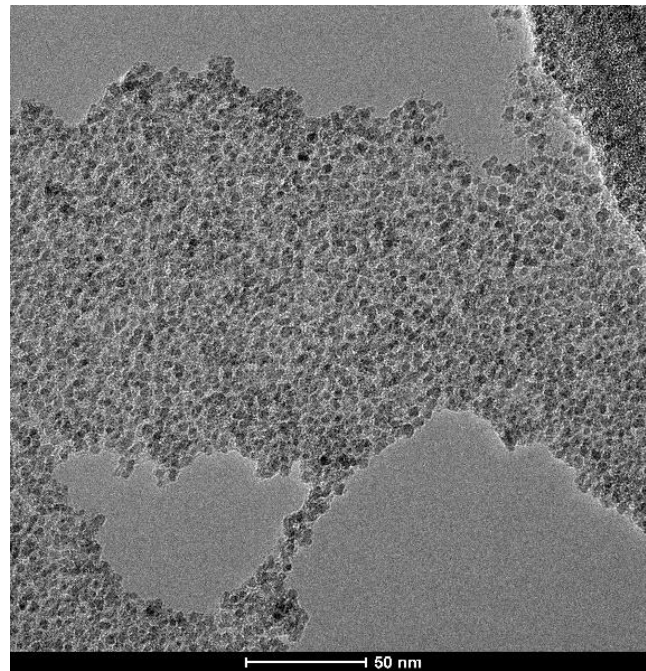


Figure 4. TEM image for ZnFe_2O_4 particles obtained at neutral pH.

3.3. Hybrid Cold-Sintered/Spark Plasma-Sintered Soft Magnetic Composite

Figure 5 shows the X-ray diffraction pattern obtained on the hybrid sintered CS-SPS for the composite compact $\text{Fe}/\text{Fe}_3\text{O}_4/\text{ZnFe}_2\text{O}_4$. It can be noticed that the sintering process led to the maintaining of the phases present in the material before sintering. According to the XRD analysis, no reaction occurred between phases during CS-SPS sintering. Fe_3O_4 and ZnFe_2O_4 have the same crystallographic structure and, therefore, their diffraction maxima almost entirely overlap at lower diffraction angles.

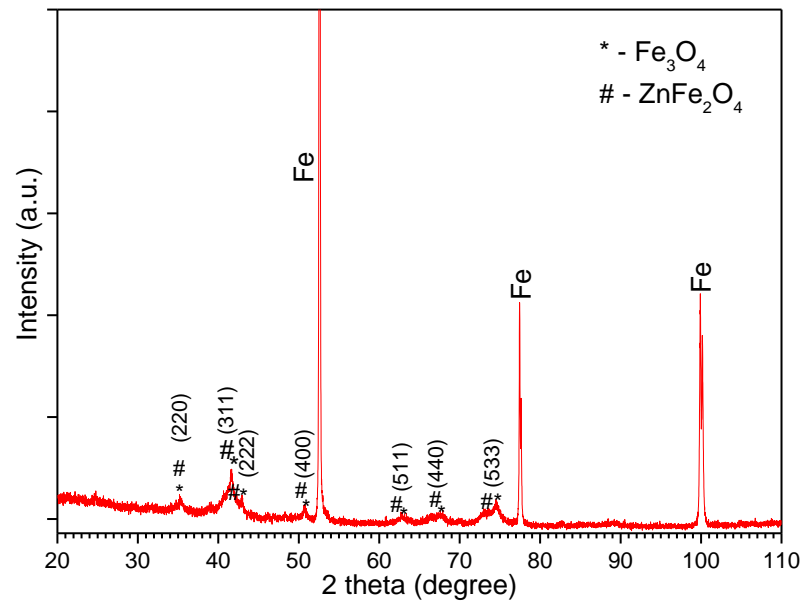


Figure 5. X-ray diffraction pattern of the compact obtained by hybrid sintering CS-SPS.

The SEM-EDX investigation of cold-sintered compact is presented in Figure 6. Analyzing the elemental distribution maps of Zn and O in the cross-section of the sample, it can be concluded that the ZnFe_2O_4 nanoparticles are distributed on the surface of the $\text{Fe}@\text{Fe}_3\text{O}_4$ particle, forming a quasi-continuous insulating layer. The uniformity of the Fe_3O_4 coating

on the surface of Fe particles cannot be evaluated by analyzing the cross-section of the cold-sintered sample since the coating contains only Fe and O atoms, and these elements are also contained by the Fe particles and ZnFe₂O₄ nanoparticles.

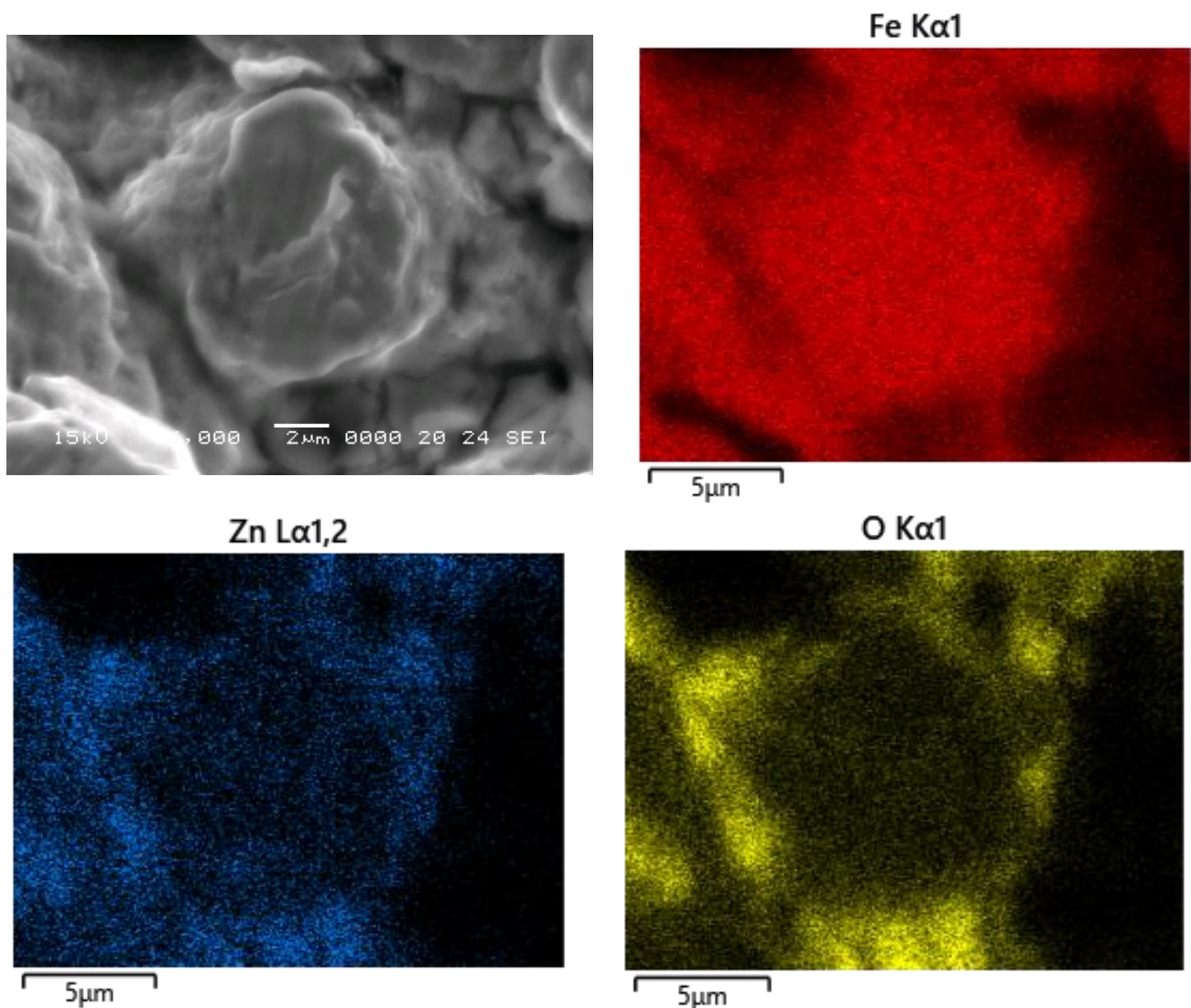


Figure 6. SEM image and elemental distribution maps (EDX) of Fe, Zn, and O on the cross-section of the composite compact prepared via a hybrid cold-sintering/spark plasma-sintering process.

The DC hysteresis loop of the composite compact is presented in Figure 7. The soft magnetic behavior of the composite magnetic core, prepared via a hybrid cold-sintering/spark plasma-sintering process, can be observed by analyzing the shape of its hysteresis curve and the values of saturation induction (B_s), remanence (B_r), coercivity (H_c), and maximum relative permeability (μ_{rmax}) provided in Figure 4. It can be noted that applying a magnetic field of 8.5 kA/m results in an induction of 0.8 T. The obtained induction value is comparable to other values reported in the literature. For example, in the case of cold-sintered compacts based on Fe powder coated with ZnO, depending on the amount of ZnO used (10–20 wt.%), a saturation induction of 0.66–0.83 T was reported [38]. The coercivity of the composite compact presented in this study (590 A/m) is higher than the coercivity reported for the above-mentioned compacts based on Fe powder coated with ZnO (469–490 A/m). The increased coercivity can be explained by the influence of the coating technique on the magnetic characteristics of the powders. The ZnO coating was prepared by immersing the Fe powder in a solution containing ZnO nanoparticles and acetic acid. No significant reaction between the base material and the coating was reported. On the other hand, the

Fe₃O₄ coating was prepared via an in situ oxidation method, which is a conversion-coating technique (the superficial metallic layer of the particles is converted into an oxide layer). An interface between the core and the shell of the particle is created during the in situ oxidation process. This interface contains a large number of pinning centers that hinder the displacement of the magnetic domain walls, thus increasing the coercivity of the powders and, consequently, the coercivity of the compact. The presence of these pinning centers also leads to a decrease in the value of the maximum relative permeability of the compact (156) compared to the value obtained in the case of cold-sintered compacts based on Fe powders coated with ZnO (174) [38].

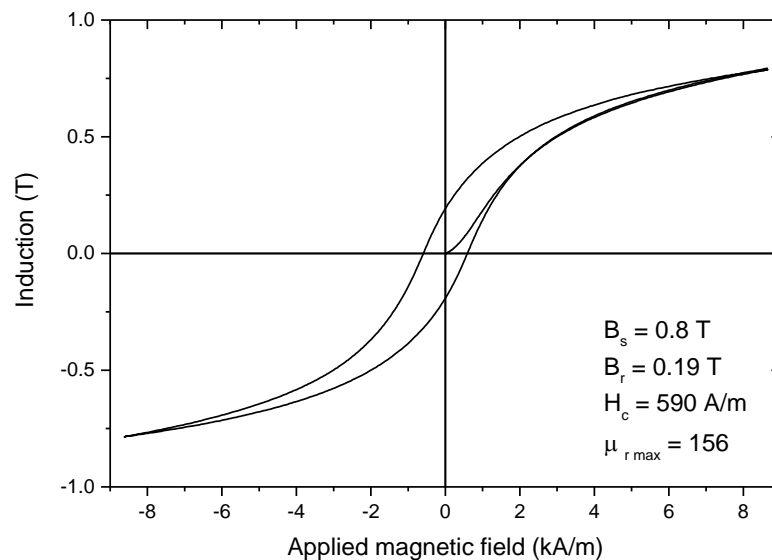


Figure 7. DC hysteresis loop of the composite compact prepared via a hybrid cold-sintering/spark plasma-sintering process.

The variation in the initial relative permeability and total core losses vs. frequency for the hybrid cold-sintered/spark plasma-sintered compact is presented in Figure 8. The value of the initial relative permeability of the compact is practically constant up to the frequency of 2 kHz. At higher frequencies, a significant decrease in the value of the permeability of the compacts is noticed. Generally, when a decrease in the value of the initial relative permeability of the SMCs is noticed, it indicates the excessive development of eddy currents in the sample. The eddy currents that circulate in the cross-section of the sample create a magnetic field that will oppose the applied magnetizing field thus reducing the permeability of the sample. The excessive development of the eddy currents in the sample is also proven by the more abrupt increase in the total core losses of the sample for frequencies higher than 1 kHz. Similar results were also reported in the case of cold-sintered SMCs based on Fe powder coated with 10 or 20 wt.% ZnO [38].

To have a better understanding of the main dissipative mechanism of our sample, a loss separation procedure was applied. The total losses of the sample (P_t) are composed of hysteresis losses (P_h), eddy current losses and excess losses (P_e) [39].

$$P_t = P_h + P_e + P_{exc}. \quad (1)$$

The contribution of the excess losses was neglected in this study since their contribution to the total losses is significant only at very high frequencies and very low induction. The eddy current losses are composed of intraparticle eddy current losses and interparticle eddy current losses. The total losses provided by Equation (4) can be written as:

$$P_s = P_h + P_e^{inter} + P_e^{intra}. \quad (2)$$

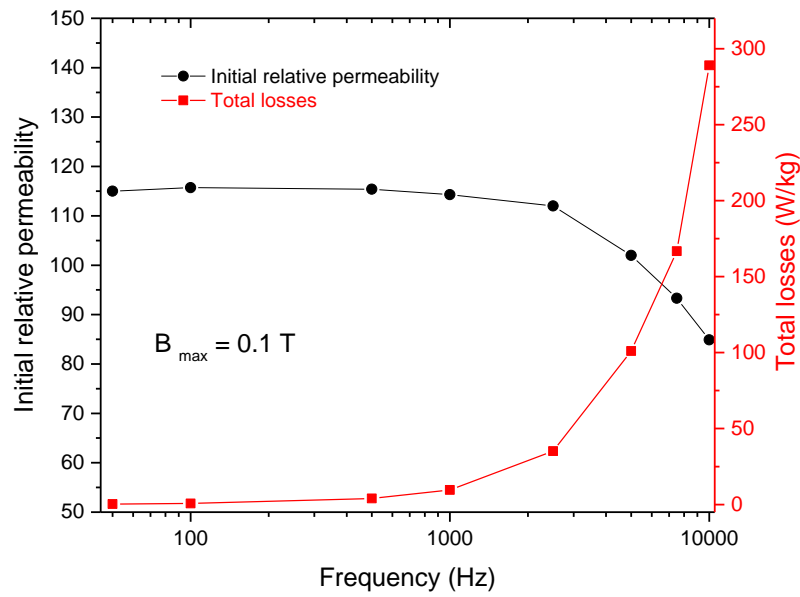


Figure 8. Initial relative permeability and total core losses vs. frequency for the hybrid cold-sintered/spark plasma-sintered compact.

Hysteresis losses are calculated by the extrapolation to 0 Hz of total losses. According to the literature, the formulas for the intraparticle and interparticle eddy current losses are [40]:

$$p_e^{intra} = \frac{(\pi d B_m)^2}{20 R_{Fe} \rho_{Fe}} f^2, \quad (3)$$

and

$$p_e^{inter} = \frac{(\pi d_{eff} B_m)^2}{\beta R_s \rho_s} f^2, \quad (4)$$

where d is the diameter of the particles, B_m is the maximum induction, f is the frequency, R_{Fe} is the specific resistivity of Fe, ρ_{Fe} is the specific density of the Fe, d_{eff} is the effective dimension for eddy current, R_s is the electrical resistivity of the sintered sample, and ρ_s represents the density of the sintered toroidal compacts. The β coefficient can be calculated using the following relation:

$$\beta = \frac{6}{1 - 0.633 \frac{w}{h} \tanh\left(1.58 \frac{h}{w}\right)}, \quad (5)$$

where w is the width of the rectangle, and h is the rectangle height (the cross-section of the sample is a rectangle).

The particle size that is used for loss separation is the median size provided by the producer of the powder; in our case, the mean particle size is 100 μm . Figure 9a presents the comparison between the measured losses and the losses calculated with this model. Good agreement between the measured and calculated losses, according to Equation (5), is obtained.

Analyzing Figure 9b, it can be observed that the value of hysteresis and dynamic losses (intraparticle and interparticle) are comparable up to the frequency of 1 kHz. At frequencies higher than 1 kHz, an excessive increase in the interparticle eddy current losses is observed. The interparticle eddy current losses become the main part of the total losses of the composite. For example, at a frequency of 10 kHz, the hysteresis losses represent approximately 0.5% of total losses, and the intraparticle eddy current losses (the eddy currents that are restrained inside individual particles) represent 2.3% of total losses of the

compact. We recall that the interparticle eddy currents are currents that develop across the boundary of the particles. The fact that, for frequencies higher than 1 kHz, this type of loss is dominant indicates that the particles are not properly insulated from each other and/or the layer thickness is not large enough to offer good electrical resistivity. Another important aspect that is necessary to be considered is that the electrical resistivity of the magnetite (iron ferrite) is much lower compared to the one of zinc ferrite ($4 \times 10^{-5} \Omega \cdot \text{m}$ for iron ferrite and $1 \Omega \cdot \text{m}$ for zinc ferrite [40]). Although the magnetite covers the iron particles well, it cannot confer a very high electrical resistivity. The large increase in interparticle losses can be associated with the inhomogeneous insulation offered by zinc ferrite nanoparticles, which possess larger electrical resistivity as compared to magnetite. Special attention must be paid to increasing the quality of the insulating coating in such a way that during the sintering procedure, the insulating coating will not be destroyed.

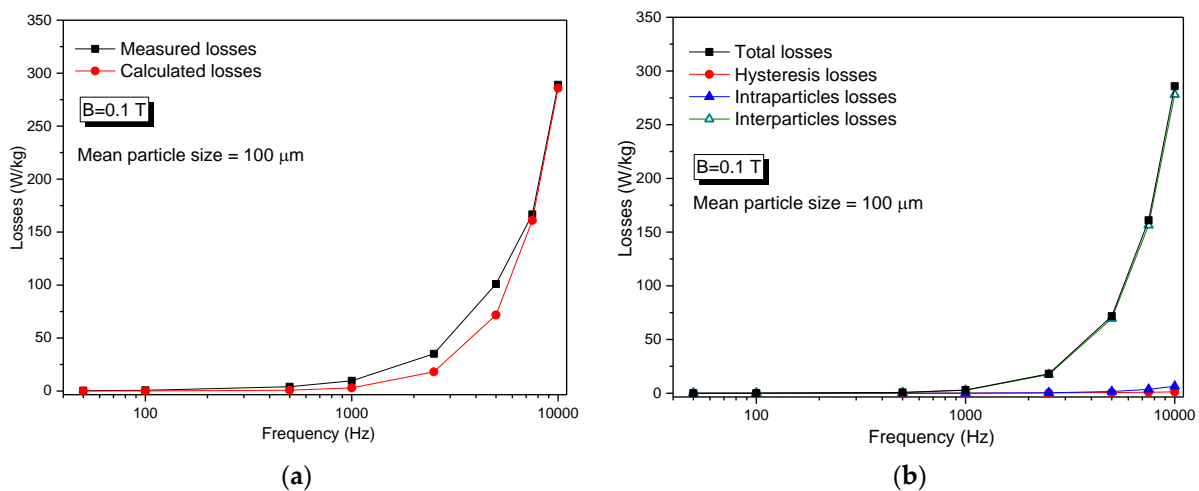


Figure 9. Results of loss separation procedure applied to the hybrid cold-sintered/spark plasma-sintered compact. (a) Comparison between measured and calculated losses. (b) Decomposition of losses in hysteresis, intraparticle, and interparticle losses.

4. Conclusions

In summary, this work allowed us to optimize the synthesis conditions for in situ oxidation of Fe particles and co-precipitation of ZnFe_2O_4 nanoparticles. $\text{Fe}@\text{Fe}_3\text{O}_4/\text{ZnFe}_2\text{O}_4$ SMC was obtained via hybrid cold-sintering/spark plasma-sintering. ZnFe_2O_4 nps were obtained using co-precipitation, a scalable method, and directly from the precipitation solution, without any thermal treatment.

XRD and FTIR measurements evidenced both the formation of an oxide layer at the surface of Fe powder and the nanosized nature of ZFNps. The SEM-EDX investigations highlighted that the oxidic phase of our composite (Fe_3O_4 and ZnFe_2O_4) was distributed on the surface of the Fe particles, forming a quasi-continuous matrix.

The DC magnetic characteristics of the composite compact were $B_s = 0.8 \text{ T}$, $H_c = 590 \text{ A/m}$, and $\mu_{r\text{max}} = 156$. The AC magnetic characterization highlighted that for frequencies higher than 1 kHz, interparticle eddy current losses were the main part of the losses as a result of insufficient insulation of neighbouring particles in the composite compact. However, the magnetic characteristics determined in both DC and AC magnetization regimes were comparable to other magnetic characteristics reported for cold-sintered Fe-based SMCs.

Author Contributions: Conceptualization, A.M., B.V.N., T.F.M. and I.C.; methodology, A.M., B.V.N., T.F.M., F.P. and G.C.; formal analysis, B.V.N., T.F.M. and F.P.; investigation, A.M., B.V.N., T.F.M., F.P. and O.R.V.; data curation, O.R.V.; writing—original draft, A.M. and B.V.N.; writing—review & editing, A.M., B.V.N., T.F.M., F.P. and I.C.; supervision, A.M. and I.C. All authors have read and agreed to the published version of the manuscript.

Funding: This work was supported by a grant from the Romanian Ministry of Education and Research, CCCDI—UEFISCDI, project number PN-III-P4-ID-PCE-2020-2264/PCE128/2021, within the PNCD III framework.

Data Availability Statement: The data presented in this study are available on request from the corresponding author.

Conflicts of Interest: The authors declare no conflict of interest.

References

1. He, J.; Yuan, H.; Nie, M.; Guo, H.; Yu, H.; Liu, Z.; Sun, R. Soft magnetic materials for power inductors: State of art and future development. *Mater. Today Electron.* **2023**, *6*, 100066. [\[CrossRef\]](#)
2. Perigo, E.A.; Weidenfeller, B.; Kollar, P.; Fuzer, J. Past, present, and future of soft magnetic composites. *Appl. Phys. Rev.* **2018**, *5*, 031301. [\[CrossRef\]](#)
3. Zhang, Q.; Zhang, W.; Peng, K. In-situ synthesis and magnetic properties of core-shell structured Fe/Fe₃O₄ composites. *J. Magn. Magn. Mater.* **2019**, *484*, 418–423. [\[CrossRef\]](#)
4. Jang, M.-S.; Park, J.-M.; Kim, J.; Sun, C.; Koo, B.; Kim, H.-R.; Kwon, Y.-T.; Yang, S.; Lee, J.W.; Kim, Y.; et al. Unprecedented heat resistance of Fe-based soft magnetic composites realized with tunable double insulation layer: Synergy of MgO diffusion barrier and void-filling SiO₂ layer. *J. Magn. Magn. Mater.* **2023**, *580*, 170893. [\[CrossRef\]](#)
5. Li, W.; Pu, Y.; Ying, Y.; Kang, Y.; Yu, J.; Zheng, J.; Qiao, L.; Li, J.; Che, S. Magnetic properties and related mechanisms of iron-based soft magnetic composites with high thermal stability in situ composite ferrite coating. *J. Alloys Compd.* **2020**, *829*, 154533. [\[CrossRef\]](#)
6. Silveyra, J.M.; Ferrara, E.; Huber, D.L.; Monson, T.C. Soft magnetic materials for a sustainable and electrified world. *Science* **2018**, *362*, 6413. [\[CrossRef\]](#)
7. Ferraris, L.; Pošković, E.; Franchini, F. New Soft magnetic composites for electromagnetic applications with improved mechanical properties. *AIP Adv.* **2016**, *6*, 056209. [\[CrossRef\]](#)
8. Li, J.; Yu, J.; Li, W.; Che, S.; Zheng, J.; Qiao, L.; Ying, Y. The preparation and magnetic performance of the iron-based soft magnetic composites with the Fe@Fe₃O₄ powder of in situ surface oxidation. *J. Magn. Magn. Mater.* **2018**, *454*, 103–109. [\[CrossRef\]](#)
9. Dobák, S.; Füzér, J.; Kollár, P.; Fáberováb, M.; Bureš, R. Interplay of domain walls and magnetization rotation on dynamic magnetization process in iron/polymer-matrix soft magnetic composites. *J. Magn. Magn. Mater.* **2017**, *426*, 320–327. [\[CrossRef\]](#)
10. Dias, M.; Mozetic, H.J.; Barboza, J.S.; Martins, R.M.; Pelegrini, L.; Schaeffer, L. Influence of resin type and content on electrical and magnetic properties of soft magnetic composites (SMCs). *Powder Technol.* **2013**, *237*, 213–220. [\[CrossRef\]](#)
11. Liu, D.; Wu, C.; Yan, M. Investigation on sol-gel Al₂O₃ and hybrid phosphate-alumina insulation coatings for FeSiAl soft magnetic composites. *J. Mater. Sci.* **2015**, *50*, 6559–6566. [\[CrossRef\]](#)
12. Zhao, W.W.; Zhang, X.K.; Xiao, J.Q. Submicrometer laminated Fe/SiO₂ soft magnetic composites—An effective route to materials for high-frequency applications. *Adv. Mater.* **2005**, *17*, 915–918. [\[CrossRef\]](#)
13. Taghvaei, H.A.; Ebrahimi, A.; Ghaffari, M.; Janghorban, K. RETRACTED: Magnetic properties of iron-based soft magnetic composites with MgO, coating obtained by sol-gel method. *J. Magn. Magn. Mater.* **2010**, *322*, 808–813. [\[CrossRef\]](#)
14. Yaghtin, M.; Taghvaei, A.H.; Hashemi, B.; Janghorban, K. Effect of heat treatment on magnetic properties of iron-based soft magnetic composites with Al₂O₃ insulation coating produced by sol-gel method. *J. Alloys Compd.* **2013**, *581*, 293–297. [\[CrossRef\]](#)
15. Geng, K.; Xie, Y.; Xu, L.; Yan, B. Structure and magnetic properties of ZrO₂-coated Fe powders and Fe/ZrO₂ soft magnetic composites. *Adv. Powder Technol.* **2017**, *28*, 2015–2022. [\[CrossRef\]](#)
16. Wu, S.; Sun, A.; Xu, W.; Zhang, Q.; Zhai, F.; Logan, P.; Volinsky, A.A. Iron-based soft magnetic composites with Mn–Zn ferrite nanoparticles coating obtained by sol–gel method. *J. Magn. Magn. Mater.* **2012**, *324*, 3899–3905. [\[CrossRef\]](#)
17. Zhong, Z.; Wang, Q.; Tao, L.; Jin, L.; Tang, X.; Bai, F.; Zhang, H. Permeability dispersion and magnetic loss of Fe/Ni_xZn_{1-x}Fe₂O₄ soft magnetic composites. *IEEE Trans. Magn.* **2012**, *48*, 3622–3625. [\[CrossRef\]](#)
18. Laxminarayana, S.K.; Manna, B.; Fernandes, N. Venkataramani, Study of AC magnetic properties and core losses of Fe/Fe₃O₄-epoxy resin soft magnetic composite. *Phys. Proc.* **2015**, *75*, 1396–1403. [\[CrossRef\]](#)
19. Sunday, J.J.; Hanejko, F.G.; Taheri, M.L. Magnetic and microstructural properties of Fe₃O₄-coated Fe powder soft magnetic composites. *J. Magn. Magn. Mater.* **2017**, *423*, 164–170. [\[CrossRef\]](#)
20. Zhao, G.; Wu, C.; Yan, M. Fe-based soft magnetic composites with high Bs and low core loss by acidic bluing coating. *IEEE Trans. Magn.* **2015**, *51*, 1–4.
21. Zhao, G.; Wu, C.; Yan, M. Enhanced magnetic properties of Fe soft magnetic composites by surface oxidation. *J. Magn. Magn. Mater.* **2016**, *399*, 51–57. [\[CrossRef\]](#)
22. Neamțu, B.V.; Pszola, M.; Opreș, A.; Popa, F.; Marinca, T.F.; Chicinaș, I. Influence of fibres diameter on the AC and DC magnetic characteristics of fibres based soft magnetic composites. *Ceramics Int.* **2021**, *47*, 1865–1874. [\[CrossRef\]](#)
23. Neamțu, B.V.; Pszola, M.; Vermeșan, H.; Stoian, G.; Grigoraș, M.; Opreș, A.; Cotojman, L.; Marinca, T.F.; Lupu, N.; Chicinaș, I. Preparation and characterisation of Fe/Fe₃O₄ fibres based soft magnetic composites. *Ceramics Int.* **2021**, *47*, 581–589. [\[CrossRef\]](#)
24. Ma, J.; Yuan, Y.; Zou, H.; Yang, B.; Zhou, B.; Yu, R. High-strength and corrosion-resistant Fe/Al₂SiO₅ soft magnetic composites fabricated by a nanoscale solid-reaction coating method. *J. Alloys Compd.* **2022**, *912*, 165174. [\[CrossRef\]](#)

25. Choi, K.D.; Lee, S.Y.; Kim, H.Y.; Hwang, J.S.; Huh, J.Y.; Yi, K.W.; Byun, J.Y. Effect of annealing on magnetic properties of iron-based soft magnetic composites with iron oxide insulator. *J. Magn. Magn. Mater.* **2022**, *562*, 169755. [[CrossRef](#)]
26. Yi, Y.; Peng, Y.; Xia, C.; Wu, L.; Ke, X.; Nie, J. Influence of heat treatment on microstructures and magnetic properties of Fe-based soft magnetic composites prepared by co-precipitation method. *J. Magn. Magn. Mater.* **2019**, *476*, 100–105. [[CrossRef](#)]
27. Peng, Y.; Nie, J.; Zhang, W.; Ma, J.; Bao, C.; Cao, Y. Effect of the addition of Al₂O₃ nanoparticles on the magnetic properties of Fe soft magnetic composites. *J. Magn. Magn. Mater.* **2016**, *399*, 88–93. [[CrossRef](#)]
28. Xiao, L.; Fan, H.; Cheng, W.; Li, Z.; Li, M. Magnetic and mechanical properties of Fe-based-Fe₂O₃/nano-sized MgO-coated composites. *Proc. Inst. Mech. Eng. Part L* **2019**, *233*, 1134–1144. [[CrossRef](#)]
29. Strečková, M.; Sopčák, T.; Medvecký, L.; Bureš, R.; Fáberová, M.; Batko, I.; Briančin, J. Preparation, chemical and mechanical properties of microcomposite materials based on Fe powder and phenol-formaldehyde resin. *Chem. Eng. J.* **2012**, *180*, 343–353. [[CrossRef](#)]
30. Marinca, T.F.; Neamțu, B.V.; Popa, F.; Mesaroş, A.Z.; Ciascai, I.; Chicinaş, I. Novel supermalloy/alumina type soft magnetic composite obtained by reaction spark plasma sintering of Al-Supermalloy (Ni70.5Fe18.8Mo4.7Al6) surface oxidized particles. *J. Alloys Compd.* **2023**, *940*, 168899. [[CrossRef](#)]
31. Nguyen, L.T.; Nguyen, K.D.M.; Nguyen, T.A.; No, K. The synthesis of zinc ferrite spinel: Determination of pH value in the co-precipitation step. *Ceram. Int.* **2022**, *48*, 4090–4095. [[CrossRef](#)]
32. Basavanagoudra, H.; Tanakanti, R.; Patil, M.K.; Inamdar, S.R.; Goudar, K.M. Synthesis, characterization, and properties of spinel zinc ferrite nanoparticles by chemical coprecipitation technique. *Macromol. Symp.* **2021**, *400*, 2100138. [[CrossRef](#)]
33. Popovici, E.J.; Muresan, L.; Hristea, A.; Indrea, E.; Vasilescu, M. Synthesis and characterisation of europium activated yttrium oxide fine powders. *J. Alloys Compd.* **2007**, *434–435*, 809–812. [[CrossRef](#)]
34. Nalbandian, L.; Patrikiadou, E.; Zaspalis, V.; Patrikidou, A.; Hatzidaki, E.; Papandreou, C.N. Magnetic Nanoparticles in Medical Diagnostic Applications: Synthesis, Characterization and Proteins Conjugation. *Curr. Nanosci.* **2016**, *12*, 455–468. [[CrossRef](#)]
35. Mesaros, A.; Ghitulica, C.D.; Popa, M.; Mereu, R.; Popa, A.; Petrisor, T.; Gabor, M.; Cadis, A.I.; Vasile, B. Synthesis, structural and morphological characteristics, magnetic and optical properties of Co doped ZnO nanoparticles. *Ceram. Int.* **2014**, *40*, 2835–2846. [[CrossRef](#)]
36. Trivedi, M.K.; Branton, A.; Trivedi, D.; Nayak, G.; Bairwa, K.; Jana, S. Spectroscopic characterization of disodium hydrogen orthophosphate and sodium nitrate after biofield treatment. *J. Chromatogr. Sep. Tech.* **2015**, *6*, 1000282. [[CrossRef](#)]
37. Ait Kerroum, M.A.; Essyed, A.; Iacovita, C.; Baaziz, W.; Ihiawakrim, D.; Mounkachi, O.; Hamedoun, M.; Benyoussef, A.; Benaissa, M.; Ersen, O. The effect of basic pH on the elaboration of ZnFe₂O₄ nanoparticles by co-precipitation method: Structural, magnetic and hyperthermia characterization. *J. Magn. Magn. Mater.* **2019**, *478*, 239–246. [[CrossRef](#)]
38. Neamțu, B.V.; Popa, F.; Marinca, T.F.; Chicinaş, I. Soft magnetic composites based on Fe fibres and powders prepared by cold sintering process. *J. Alloys Compd.* **2023**, *933*, 167799. [[CrossRef](#)]
39. Kollár, P.; Birčáková, Z.; Füzér, J.; Bureš, R.; Fáberová, M. Power loss separation in Fe-based composite materials. *J. Magn. Magn. Mater.* **2013**, *327*, 146–150. [[CrossRef](#)]
40. Goldman, A. *Modern Ferrite Technology*, 2nd ed.; Springer: Pittsburgh, PA, USA, 2006.

Disclaimer/Publisher’s Note: The statements, opinions and data contained in all publications are solely those of the individual author(s) and contributor(s) and not of MDPI and/or the editor(s). MDPI and/or the editor(s) disclaim responsibility for any injury to people or property resulting from any ideas, methods, instructions or products referred to in the content.